A Generalized Method for Calculating Atmospheric Ionization by Energetic Electron Precipitation

Wei Xu,[1] Robert A. Marshall,[1] Hilde Nesse Tyssøy,[2] and XiaoHua Fang[3]

[1]Department of Aerospace Engineering Sciences, University of Colorado Boulder, Boulder, CO, USA.
[2]Birkeland Centre for Space Science, Department of Physics and Technology, University of Bergen, Bergen, Norway.
[3]Laboratory for Atmospheric and Space Physics, University of Colorado Boulder, Boulder, Colorado, USA.

Key Points:

- We tabulate the atmospheric ionization response to monoenergetic beams of precipitating electrons with different pitch angles
- We report a method to derive the ionization profile under any Earth atmosphere condition by any electron energy and pitch angle distribution
- This method provides a reliable means to convert space measurements of precipitation into ionization input in atmospheric chemistry modeling

Corresponding author: Wei Xu, Wei-Xu@colorado.edu

Abstract

Accurate specification of ionization production by energetic electron precipitation is critical for atmospheric chemistry models to assess the resultant atmospheric effects. Recent model-observation comparison studies have increasingly highlighted the importance of considering precipitation fluxes in the full range of electron energy and pitch angle. However, previous parameterization methods were mostly proposed for isotropically-precipitation electrons with energies up to 1 MeV and the pitch angle dependence has not yet been parameterized. In this paper, we first characterize and tabulate the atmospheric ionization response to monoenergetic electrons with different pitch angles and energies between ~3 keV and ~33 MeV. A generalized method that fully accounts for the dependence of ionization production on background atmospheric conditions, electron energy, and pitch angle has been developed based on the parameterization method of ***Fang et al.*** [2010]. Moreover, we validate this method using 100 random atmospheric profiles and precipitation fluxes with monoenergetic and exponential energy distributions, and isotropic and sine pitch angle distributions. In a suite of 6,100 validation tests, the error in peak ionization altitude is found to be within 1 km in 91% of all the tests with a mean error of 2.7% in peak ionization rate, and 1.9% in total ionization. This method therefore provides a reliable means to convert space-measured precipitation energy and pitch angle distributions into ionization inputs for atmospheric chemistry models.

1 Introduction

Energetic particle precipitation (EPP) causes significant disturbances to the entire magnetosphere-ionosphere-atmosphere system, including the dynamics of the radiation belts [e.g., ***Lyons and Thorne***, 1973] and the thermal, electrical [e.g., ***Mironova et al.***, 2015], and chemical [e.g., ***Sinnhuber et al.***, 2012] properties of the Earth's atmosphere [e.g., ***Marshall and Cully***, 2020]. Of particular relevance to our living environment is the direct influence on ozone concentration in the stratosphere and mesosphere [e.g., ***Thorne***, 1980; ***Randall et al.***, 2007; ***Sinnhuber et al.***, 2012]. Through efficient ionization interactions, EPP results in production of reactive odd nitrogen (NO_x) [e.g., ***Rusch et al.***, 1981] and odd hydrogen (HO_x) [e.g., ***Solomon et al.***, 1981] in the atmosphere. The short-lived HO_x compounds can locally deplete the ozone concentration by as large as 90% [***Andersson et al.***, 2013] in the mesosphere. NO_x compounds in the absence of sunlight can have a lifetime of months. If trapped inside the winter polar vortex, the NO_x gas will be transported downward from the lower thermosphere to the stratosphere by the residual circulation which has a descending branch over the winter pole, thereby accelerating the catalytic ozone destruction cycle [***Callis et al.***, 1998; ***Randall et al.***, 2007]. The ozone losses induced by EPP have indirect implications for radiative balance, cloud formation, atmospheric electricity, and circulation of the upper and middle atmosphere [e.g., ***Sinnhuber et al.***, 2012; ***Rozanov et al.***, 2012; ***Mironova et al.***, 2015].

In spite of extensive theoretical and observational efforts, the atmospheric chemistry effects caused by EPP are still not fully understood [e.g., ***Sinnhuber et al.***, 2012; ***Mironova et al.***, 2015]. Precipitating auroral electrons are often isotropic in pitch angle, have energies ranging from a fraction to a few tens of keV, and deposit most of their energies in the lower thermosphere in the auroral oval region. The resultant chemical changes are found to be positively correlated with the intensity of geomagnetic activity [e.g., ***Baker et al.***, 2001; ***Barth et al.***, 2003; ***Marsh et al.***, 2007]. On the other hand, the chemical effects produced by more energetic electron precipitation (EEP) are less well understood [e.g., ***Sinnhuber et al.***, 2012; ***Mironova et al.***, 2015]. This is partially due to the variability of precipitation fluxes in electron energy and pitch angle, as caused by repetitive particle acceleration/deceleration and pitch-angle scattering during wave-particle interactions. Therefore, while evaluating EEP-induced effects, it is of essential importance to convert

these highly variable precipitation fluxes into an accurate ionization source in atmospheric chemistry models.

Accurate specification of ionization production requires consideration of precipitation fluxes in the full range of electron energy and pitch angle, a point that has been repeatedly raised in recent model-observation comparison studies [e.g., ***Randall et al.***, 2015; ***Nesse Tyssøy et al.***, 2016; ***Smith-Johnsen et al.***, 2018; ***Pettit et al.***, 2019]. In particular, ***Randall et al.*** [2015] analyzed the NO_x enhancements produced by an intense EPP event during the 2003–2004 Arctic winter. However, numerical simulations using the Whole Atmosphere Community Climate Model with Specified Dynamics (SD-WACCM) provided inconsistent results with satellite measurements; modeling results underestimated the NO_x fluxes by at least a factor of four. The reason, as suggested by ***Randall et al.*** [2015], was the inaccurate transport rate adopted in SD-WACCM, as well as not including high-energy precipitating electrons.

The studies of ***Nesse Tyssøy et al.*** [2016] and ***Pettit et al.*** [2019] not only confirmed this finding, but also highlighted the role of pitch angle distribution. By fitting the pitch angle distribution from the theory of wave-particle interactions, ***Nesse Tyssøy et al.*** [2016] combined measurements from the two telescopes (0° telescope: pointing close to the zenith; 90° telescope: pointing close to the horizon) of the Medium Energy Proton and Electron Detector (MEPED) onboard the Polar Orbiting Environmental Satellites (POES), and derived a complete distribution of loss cone fluxes in both energy and pitch angle. The authors have further verified this distribution using OH measurements by the Microwave Limb Sounder onboard the Aura satellite, and revealed that the comparison with observational data achieved good agreements only after taking the full pitch angle distribution into account.

Pettit et al. [2019] performed detailed comparison between NO_x measurements during the Austral winter in 2003 and WACCM simulations using two different sets of precipitation data: one set of the data only included particle measurements from the 0° telescope of MEPED, while the other one incorporated measurements from both telescopes. It has been clearly demonstrated that including more information of precipitation pitch angle, as in the latter set of simulations, greatly improves the agreements with NO_x observation at middle latitudes. Despite these findings, there does not exist to date a reliable method to convert precipitation distributions into atmospheric ionization rate profiles: previous parameterization methods were mostly proposed for precipitation electrons with energies up to 1 MeV [***Fang et al.***, 2008, 2010], and the dependence on pitch angle has been largely overlooked.

Numerous methods have been established for atmospheric ionization production by EEP using range calculations [***Spencer***, 1959; ***Lazarev***, 1967; ***Roble and Ridley***, 1987; ***Lummerzheim***, 1992]. The methods of ***Spencer*** [1959] and ***Lazarev*** [1967] were developed by scaling laboratory measurements of electron energy absorption function to the atmosphere. These methods have been extended by ***Roble and Ridley*** [1987] to calculate the ionization of Maxwellian-distributed precipitating electrons, but only for the pitch angle of zero degree, and later by ***Lummerzheim*** [1992] to calculate the ionization for several predefined pitch angle distributions. Nevertheless, these methods were derived using simplified range calculations and the accuracy is limited at low energies and highly anisotropic pitch angles [e.g., ***Solomon***, 2001], therefore no longer adequate in recent model-observation comparison studies.

More rigorous parameterization methods have been proposed using physics-based models for a Maxwellian energy distribution [***Fang et al.***, 2008], and for monoenergetic electrons [***Fang et al.***, 2010]. Both methods have only parameterized precipitating electrons with energies less than 1 MeV and with an isotropic pitch angle distribution; the recently-emphasized pitch angle dependence was not considered. Using the Cosmic Ray Atmospheric Cascade (CRAC) model [e.g., ***Artamonov et al.***, 2016], ***Artamonov et al.***

[2017] have performed detailed studies on the atmospheric ionization by electrons with non-vertical precipitation. However, the ionization yield function for non-vertical precipitation electrons was not obtained from first-principles approach and how the yield function can be applied to different background atmospheres was not explained. The necessity to fully characterize the dependence of ionization production on the energy and pitch angle of precipitating electrons, as well as the background atmospheric condition, motivate the present work to extend the parameterization method of ***Fang et al.*** [2010]. The goal is to establish a robust generalized method for the specification of ionization profiles in any Earth atmosphere by precipitating electrons with any distribution in energy and pitch angle, with a view of providing a reliable ionization source to the modeling of EEP-induced atmospheric effects.

2 Model and Methodology

In this work, we calculate the impact ionization from precipitating energetic electrons using a first-principles model: the Energetic Precipitation Monte Carlo (EPMC) model, originally developed by ***Lehtinen et al.*** [1999] and modified by our group at CU Boulder over the past few years. A brief description of this model is given in section 2.1. In section 3.2, we introduce a lookup table, i.e., atmospheric response functions in terms of ionization production to monoenergetic electrons with discrete energies and pitch angles. We elucidate, in section 2.3, how to convert this lookup table from its default background atmosphere to a new atmosphere, and, in section 2.4, how to calculate the altitude profile of ionization production by precipitation electrons with arbitrary distribution in energy and pitch angle. In section 2.5, we explain the numerical error determined by validation testing. Moreover, we validate this method, in section 3, through its application to monoenergetic and exponential energy distributions in 100 different atmospheres, and isotropic and sine pitch angle distributions.

2.1 Energetic Precipitation Monte Carlo Model

The EPMC model was originally developed by ***Lehtinen et al.*** [1999] for studies of energetic radiation from thunderstorm activity, and has been recently adapted to simulate EEP effects [e.g., ***Marshall et al.***, 2014; ***Xu et al.***, 2018; ***Marshall and Bortnik***, 2018] since the underlying electron/photon collisional processes are similar. The details of this model have been described earlier [e.g., ***Lehtinen et al.***, 1999; ***Marshall et al.***, 2014]. In short, this model explicitly solves the equation of electron motion at the microscopic level using the stopping power and Möller cross section. The angular diffusion is mostly due to elastic scattering by ambient neutral species and the resultant change in momentum direction and magnitude is modeled using the method of small-angle collisions [***Lehtinen***, 2000, pp. 15–18]. As a built-in feature, this model outputs height-resolved energy deposition, and ionization production is then derived from energy deposition by assuming that an average energy of ~35 eV is needed to produce an ion-electron pair [***Rees***, 1989, p. 40]. We emphasize that this model has been validated in the past few decades in a variety of studies, including gamma-ray emissions produced by lightning discharge [***Lehtinen et al.***, 1999], interaction of a beam of relativistic electrons with the atmosphere [***Marshall et al.***, 2014], bremsstrahlung effects in EEP [***Xu et al.***, 2018; ***Xu and Marshall***, 2019], and lightning-induced electron precipitation [***Marshall et al.***, 2019].

This model can adopt arbitrary background mass density profile and magnetic field as input. In this work, the background magnetic field is assumed to be vertical with a magnitude typical of that at around 700 km altitude at Poker Flat, Alaska at nighttime (41,528 nT). Magnetic mirroring due to the magnetic gradient force is included in the model [***Lehtinen***, 2000, pp. 108–109]. The background profiles of neutral atmosphere are obtained from the NRLMSISE-00 model [***Picone et al.***, 2002]. A total of 100 MSIS atmospheric profiles are generated (see Figure 3e) and used in validation testing (section 3).

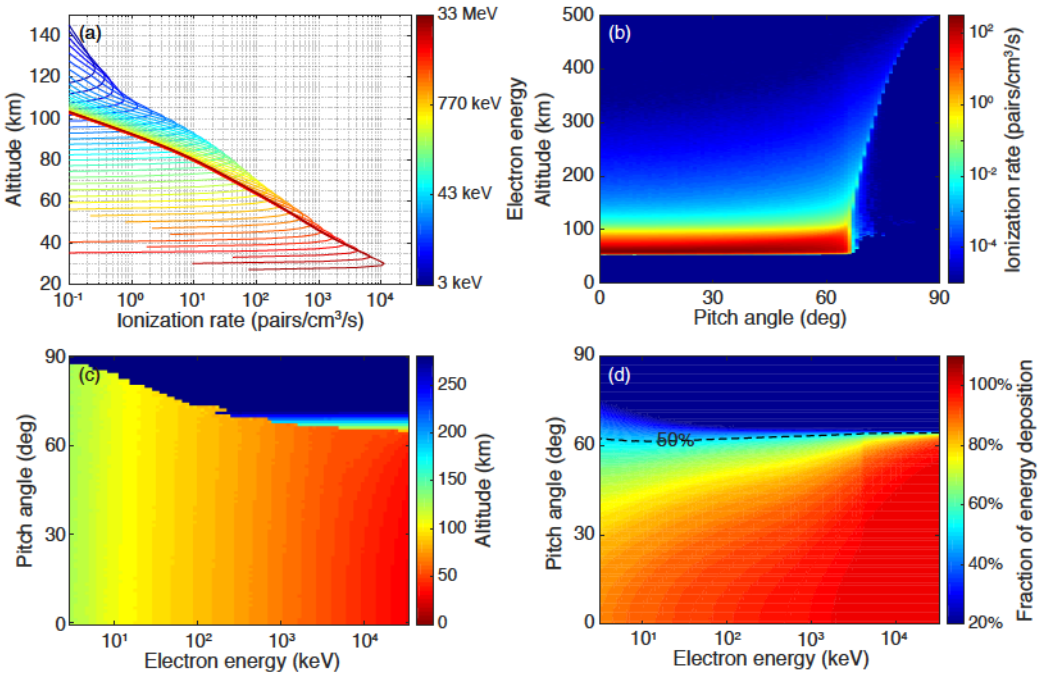

Figure 1. (a) Ionization production at altitudes between 20 and 150 km by monoenergetic beams of precipitating electrons with an incident pitch angle of 0°, and with energies between ~3 keV and ~33 MeV. The number flux of source electrons used in this set of simulations is assumed to be 10^4 el/cm^2/s. (b) Ionization production by 1 MeV electrons with pitch angles (at 500 km altitude) varying from 0° to 90°. (c) Altitude of peak ionization production by monoenergetic beams of precipitating electrons with different energies (3 keV–33 MeV) and pitch angles (0°–90°). (d) The fraction of total precipitation energy deposited in the atmosphere.

These profiles are obtained for years between 1990 and 2019 with random combinations of latitude and longitude, and with a broad coverage of $F_{10.7}$ (50–300 sfu) and A_p values (0–40 nT).

2.2 Lookup Table: Atmospheric Ionization by Monoenergetic Electrons with Different Pitch Angles

The EPMC model is employed to calculate a lookup table of ionization rate as a function of altitude produced by monoenergetic electrons with discrete pitch angles. Specifically, monoenergetic beams of energetic electrons are assumed to precipitate into the upper atmosphere from an altitude of 500 km. This altitude is chosen from the following considerations: 1) it is far above the interaction region between precipitation electrons and air molecules under most atmospheric conditions; 2) computation time; 3) it is close to that of a future EEP-observing CubeSat mission: the Atmospheric Effects of Precipitation through Energetic X-rays (AEPEX) mission [***Marshall et al.***, 2020]. The background atmosphere utilized in the lookup-table calculation (black curve in Figure 3e) is calculated using the NRLMSISE-00 model with $F_{10.7}$ = 200 sfu and A_p = 15 nT. The electron energies are roughly uniformly distributed in the logarithmic space; 91 energy values spanning from 3 keV to 33 MeV are chosen (see Figure 1); the specific choice of electron energies is not critical as long as sufficient energy values are used to provide a good resolution of ionization production at altitudes between 30 and 120 km; the number flux of precipitat-

ing electrons is assumed to be 10^4 el/cm^2/s in the downward hemisphere [e.g., ***Whittaker et al.***, 2013]. For the sake of consistency, this flux number is used throughout this work for source electrons in Monte Carlo simulations.

For each energy, we vary the input pitch angle (at 500 km altitude) from 0° to 90° with 1° step. This range of electron energy and pitch angle is chosen based on two considerations. First, it ensures a good resolution of ionization rate at altitudes of interest in studies of atmospheric chemical changes. Second, it provides a broad coverage over the detection capability of present space-borne instruments. Ionization production is theoretically governed by the background atmospheric conditions, precipitation energy and pitch angle, and the background magnetic field. Due to the complexity of this problem, the dependence on background magnetic field is not considered in the present study. ***Cotts*** [2011] have specifically investigated the dependence of ionization production on geomagnetic filed dip angle and found that the effects are not significant (not larger than 10%). The monoenergetic simulation results are summarized in Figure 1.

Figure 1a shows the ionization production at altitudes between 20 and 150 km by monoenergetic electrons with energies between ~3 keV and ~33 MeV when vertically incident on the atmosphere. It is clear that the penetration depth increases with precipitation energy, roughly linearly with the logarithmic value of the incident energy. Figure 1b shows the ionization production by 1 MeV electrons with pitch angles varying from 0° to 90°. With an initial altitude of 500 km, the nominal loss cone angle is ~66° based on a loss cone defined by a mirror altitude of 100 km. Electrons with larger pitch angle are mirrored before reaching 100 km altitude and only a small portion of precipitation energy is dissipated (see Figure 1b).

Figure 1c shows the altitude of peak ionization production for different precipitation energies and pitch angles, while Figure 1d shows the fraction of total precipitation energy deposited in the atmosphere. As the electron energy increases from 3 keV to 33 MeV, the fraction of energy deposition gradually increases since electrons become more penetrating and can thus interact with denser atmosphere at relatively lower altitudes. The sharp edge in Figure 1d around 65° (dashed line) roughly depicts how the loss cone angle changes with electron energy, which is roughly consistent with the results reported in ***Marshall and Bortnik*** [2018]. Note that this line does not specifically show the bounce loss cone angle.

2.3 Converting the Lookup Table to A New Atmosphere

To infer the ionization profile in a new independent atmosphere (denoted as the new atmosphere hereafter), we convert the lookup table using its background atmosphere (denoted as the reference atmosphere hereafter, black line in Figure 3e) in four steps. First, we cumulatively sum the mass density and ionization rate in the reference atmosphere from the starting altitude (500 km) down to the altitude at which electrons are completely absorbed by the atmosphere. This step is largely motivated by the parameterization scheme described in ***Fang et al.*** [2010] as the authors transformed ionization results into two normalized quantities: energy dissipation versus a power law of column mass density. Figure 2 shows two examples of how to convert the lookup table from its default background atmosphere to a new atmosphere, for 3 keV (the minimum energy in our lookup table) and 773 keV electrons. In the following, we use the 3-keV case as an example to explain this conversion method. The black curve in Figure 2a shows the column mass density that 3 keV electrons propagate through in the reference atmosphere, while the black curve in Figure 2b shows the cumulative sum of ionization rate versus altitude.

Second, we determine the lowest altitude of ionization in the new atmosphere by finding out the altitude above which the column mass density is similar to what electrons traverse in the reference atmosphere. For example, in the reference atmosphere, a 3-keV electron is absorbed at ~112 km altitude by a column mass density of 5.9×10^{-8} g/cm^2

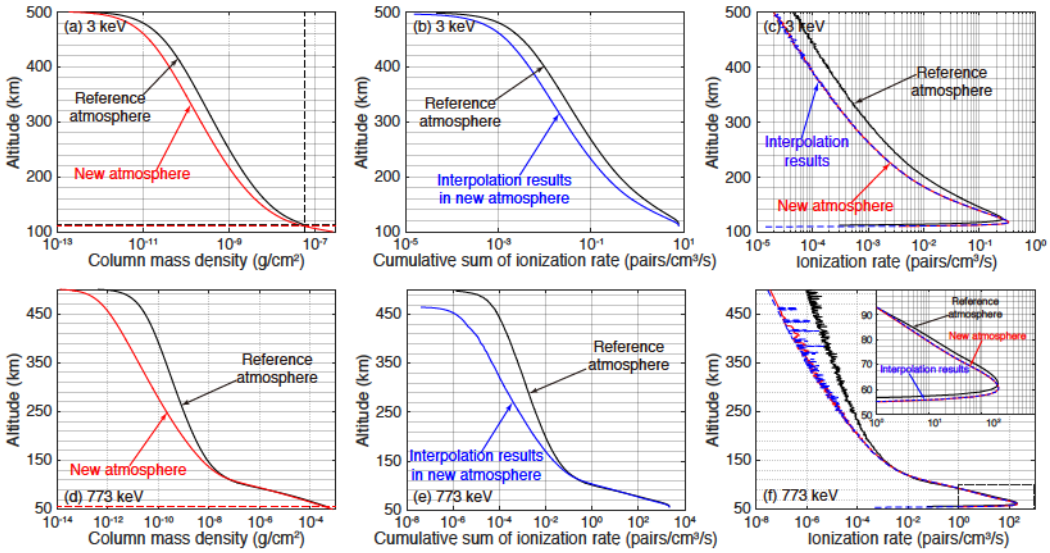

Figure 2. (a) Column mass density that 3 keV electrons with a pitch angle of 0° propagate through. The horizontal dashed lines delineate the lowest altitude of ionization production. (b) Cumulative sum of ionization rate in the reference atmosphere (black curve) and interpolation results of cumulative ionization in the new atmosphere (blue curve). (c) Comparison of ionization profile produced by 3 keV electrons between direct Monte Carlo results (red curve) and interpolation results (blue curve). The bottom panels show similar results, but for 773 keV electrons.

(black dashed line in Figure 2a), corresponding to the total mass density above ~110 km in the new atmosphere (red dashed line in Figure 2a). Thus, a 3-keV electron would most likely stop around 110 km altitude in the new atmosphere and this is the lowest altitude of ionization production. However, this is not the "perfect" lowest altitude: because of the variation in background density and resolution in altitude, we cannot find an altitude above which the column mass density is exactly the same as that in the reference atmosphere. Instead, the first altitude grid point (starting from the upper boundary) above which the column mass density is larger than that in reference atmosphere is chosen to be the lowest ionization altitude. As will be explained later, this approximation introduces a small numerical error in our validation test. This error can be reduced by using a better method to determine the lowest ionization altitude in new atmosphere or using finer grid cells in altitude. The development of a better method/algorithm is left for future work.

Using the column mass density in the reference and new atmospheres (black and red curves in Figure 2a), we further interpolate the cumulative sum of ionization rate from the upper boundary down to the lowest ionization altitude in reference atmosphere (black curve in Figure 2b); the cumulative sum of ionization rate versus altitude in the new atmosphere is obtained (blue curve in Figure 2b). Finally, we differentiate the interpolation results and calculate the ionization rate at each altitude; the results are then altitude profile of ionization rate, and shown as the blue curve in Figure 2c. The new atmospheres in Figures 2c and 2f are randomly chosen from the 100 MSIS atmospheres (Figure 3e) used in validation test. Note that the column mass density exhibits great variation at altitudes above ~200 km in different atmospheres (see Figure 3e). Since we interpolate in column mass density, the interpolation results of cumulative ionization in new atmosphere usually do not start from the same altitude of reference atmosphere (blue and black curves in Figure 2e); in this case, we extrapolate the ionization profile up to 500 km altitude.

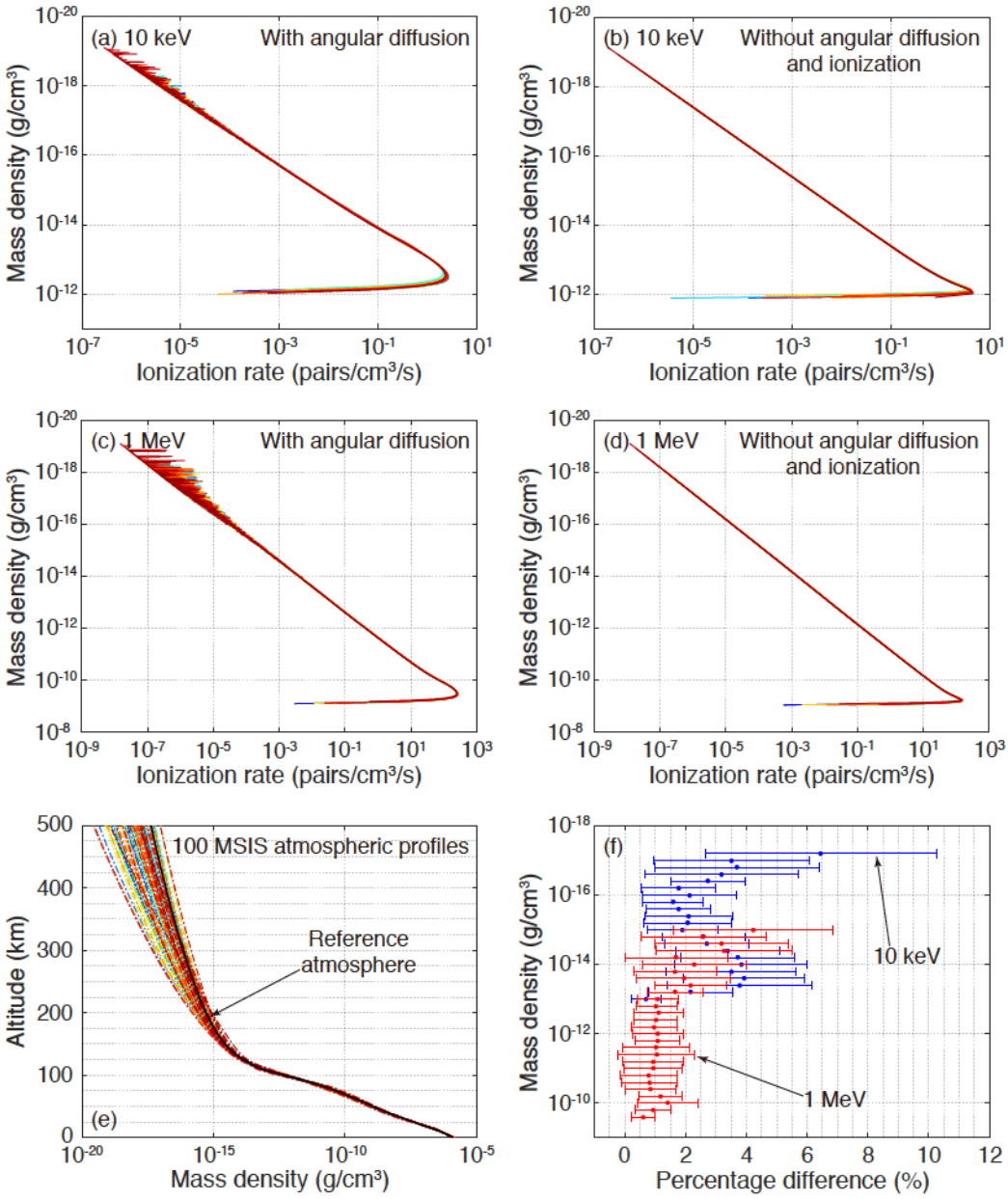

Figure 3. Altitude profile of ionization production in 20 MSIS atmospheres by 10 keV electrons with a pitch angle of 0° (a) with and (b) without considering angular diffusion and ionization production in Monte Carlo simulations. The source precipitation flux is 10^4 el/cm^2/s. Panels (c) and (d) show similar results, but for 1 MeV electrons. (e) Mass density versus altitude for 100 MSIS atmospheric profiles. (f) Percentage difference from the mean value of ionization rate versus mass density for 10 keV and 1 MeV electrons.

To validate this interpolation method, we have directly calculated the true ionization in the new atmosphere using a direct Monte Carlo simulation in the new atmosphere, and these results are shown as red curves in Figures 2c and 2f. Clearly, one sees that the interpolated profiles are extremely close to the true ionization for both energies. The error between direct Monte Carlo results (red curve) and interpolation results (blue curve) is, on average, 3.9% and 22% for the precipitation energy of 3 keV (Figure 2c) and 773 keV (Figure 2f), respectively. Particularly for the energy of 773 keV, this method not only reproduces the ionization over an altitude range of 450 km, but the altitude and magnitude of peak ionization as well (see the inset of Figure 2f).

2.4 Atmospheric Ionization by Arbitrary Distribution in Electron Energy and Pitch Angle

Having obtained the lookup table in the new atmosphere, the ionization profile produced by an arbitrary distribution of electron energy and pitch angle can be calculated as a weighted sum of the ionization contribution from each energy and pitch angle component [e.g., ***Fang et al.***, 2010; ***Berger and Seltzer***, 1972]. Specifically, we construct the ionization profile using the following formula:

$$I = \sum_{\varepsilon_{\min}}^{\varepsilon_{\max}} \sum_{0^\circ}^{90^\circ} I_0(\varepsilon,\alpha) f(\varepsilon,\alpha) \Delta\alpha \Delta\varepsilon \tag{1}$$

where $I_0(\varepsilon,\alpha)$ is the interpolated lookup table in the new atmosphere, which contains the ionization rate versus altitude produced by electrons with an energy ε and a pitch angle α, $\varepsilon_{\min}$ and $\varepsilon_{\max}$ are the lowest and highest electron energy, $\Delta\alpha$ is the width of pitch angle bins, and $\Delta\varepsilon$ is the width of energy bins, and $f(\varepsilon,\alpha)$ is the differential number flux of precipitation electrons in energy and pitch angle. In the following validation test (section 3), we assume that the energy and pitch angle distributions are not coupled; but this assumption is unnecessary in the analysis of real measurements and the ionization profile can be explicitly calculated using equation 1, where $f(\varepsilon,\alpha)$ may define a coupled energy-pitch angle dependence.

2.5 Numerical Error in Validation Test

We validate the above-mentioned lookup table and interpolation method in section 3. In this section, we explain the numerical error involved in validation testing. As the foundation of the electron transport model, the stopping power describes the effect of the medium in slowing down the projectile and is usually expressed in energy loss per unit distance or mass traversed [e.g., ***Carron***, 2006]. For the same precipitation energy, within the continuous slowing down range, energy deposition scales in theory as the mass density that the electron encounters, so is the rate of ionization interaction. However, the input of atmospheric chemistry models is usually in the form of ionization production per unit altitude of travel, which is not the same as the distance traversed by a precipitating electron due to its non-zero pitch angle. Hence, the ionization profile does not scale strictly with the background mass density.

The altitude profile of ionization rate is determined as much by ambient mass density as by angular diffusion (defined herein as the change in direction of propagation due to collisions between electrons and air molecules, e.g., elastic scattering, ionization collision, and excitation collision), especially at low energies. A single electron does not always follow the same gyromotion before stopping power brings it to rest and its trajectory is likely tortuous. Collisions with air molecules result in a change of electron energy and random scattering results in a change of pitch angle; both interrupt the gyromotion and the amount of mass density that the electron traverses in unit altitude. The rate of energy absorption and ionization production would be accordingly enhanced or suppressed. This

statement also holds for a limited number of electrons propagating in low-density region, for example, present Monte Carlo simulations at high altitudes, wherein angular diffusion by air molecules is infrequent and the resultant change in ionization rate is highly non-linear and unpredictable. This is the main cause of variation in the ionization profiles at relatively high altitudes (>150 km), as evidenced by the results shown in Figure 3.

Figure 3a shows the ionization profiles produced by 10-keV electrons in 20 different MSIS atmospheres versus the corresponding mass density above the ionization peak. These atmospheres are the first 20 of the 100 MSIS profiles used in validation test (Figure 3e). Figure 3b shows similar results, but obtained by turning off the angular diffusion and ionization production term in Monte Carlo simulations. The main difference between these two plots is that the ionization curves in Figure 3b lie nearly on top of the darkest red curve at densities below 6×10^{-13} g/cm^3 (lower density corresponds to higher altitude). Without angular diffusion and ionization production, the ionization profiles are much less spread, as being roughly proportional to the mass density. It is thus conceivable that, if ionization profiles in different atmospheres are well normalized to the mass density, like those in Figure 3b, we can simply pick any of these curves as reference, interpolate in mass density, and precisely derive the ionization profile in other atmospheres. However, in Monte Carlo simulations with a limited number of particles, angular diffusion and ionization production adds some randomness to these otherwise well-normalized ionization curves (Figure 3b) and this is the origin of numerical error in our validation test (Section 3).

These randomness effects are less pronounced at higher precipitation energies. Similar results for 1 MeV electrons are presented in Figures 3c and 3d. Contrary to the 10 keV results, the 1-MeV ionization curves lie close together at densities greater than $\sim10^{-14}$ g/cm^3. The reason is that angular diffusion at high-density altitudes is frequent and, for an ensemble of electrons, its impact on ionization rate becomes more deterministic. A better illustration of this point is shown in Figure 3f. For both 10 keV and 1 MeV electrons, we first simulate the ionization profiles in 100 different atmospheres; the mean value of ionization rate in these atmospheres is derived as a function of background density; we then compute the percentage difference of each ionization profile from the mean value. The average value of percentage difference versus mass density is presented in Figure 3f with error bars showing one standard deviation. Above the ionization peak, the percentage difference becomes smaller with increasing mass density and is notably larger for 10 keV electrons than 1 MeV. This figure shows a quantitative measure of the variation and represents the inherent error in our validation test.

3 Validation and Error Analysis

We have performed a total of 6,100 tests using 100 MSIS atmospheric profiles (Figure 3e) in order to examine the robustness of our method. These tests are categorized into three different sets of energy and pitch angle distributions at the initial altitude of EPMC simulations (500 km): 1) monoenergetic beams of electrons with a pitch angle of 0°; 2) isotropic distributions in pitch angles between 0° and 90°, and exponential energy distributions in the range from 10 keV to 10 MeV: $f(\varepsilon) \propto \exp(-\varepsilon/\varepsilon_0)$, where ε_0 is the characteristic energy of electron distribution; and 3) exponential distributions in energy and sine distributions in pitch angle: $f(\alpha) \propto \sin(\alpha)$, where α is the pitch angle (between 0° and 90°; 0° means propagating vertically downward) at 500 km altitude. The first set of monoenergetic tests is conducted mainly to verify the above-mentioned interpolation method. Space-borne measurements commonly reveal an exponential energy distribution for EEP [e.g., ***Whittaker et al.***, 2013; ***Breneman et al.***, 2017] and this is the main focus of our validation test. The last set of energy and pitch angle distributions is more realistic and the second set is utilized for the sake of completeness and for the comparison with ***Fang et al.*** [2010].

Note that it is commonly assumed that the pitch angle distribution at the equator follows the Vampola's equation [***Vampola***, 1997]: precipitation flux varies with the pitch angle as sine to the power of n. The specific choice of n value in Vampola's equation is not critical in present study and we opt to assess the performance of this lookup table in the simplest scenario (n = 1). As in EPMC simulations, we do not consider the change of pitch angle distribution due to change in background geomagnetic field. However, one can always map the pitch angle distribution of satellite-measured precipitation fluxes from its location to the initial altitude of present lookup table using the background geomagnetic field.

In the monoenergetic test, we use 19 electron energies that are uniformly distributed in the logarithmic scale between 3 keV and 33 MeV. Typical space-measured ε_0 values are in the range of 70–500 keV [e.g., ***Whittaker et al.***, 2013; ***Crew et al.***, 2016; ***Breneman et al.***, 2017]. Therefore, for the exponential distribution, 21 ε_0 values uniformly spaced in the logarithmic scale from 10 keV to 1 MeV are utilized. We conduct 100 Monte Carlo runs for each ε_0 value and each monoenergetic test using 100 MSIS profiles as the background atmosphere. The ionization results of these runs are employed as truth data against which the ionization derived from the lookup table can be evaluated. The ideal scenario is to verify the lookup-table calculation using real measurements, but the resolution of precipitation measurements and the lack of reliable observational data prevent us from performing such comparisons.

By measuring the difference from the truth, we estimate the error of derived ionization profile mainly in three aspects: peak ionization altitude, peak ionization rate, and total ionization, similar to those in ***Fang et al.*** [2010]. Note that the lookup table and truth data in validation tests are both calculated using the EPMC model, which has been validated in a variety of studies. In the following, we validate this model again through comparison with ***Fang et al.*** [2010] in section 3.1, and evaluate the performance of above-mentioned lookup table in sections 3.2, 3.3, and 3.4.

3.1 Comparison with the Parameterization Method of *Fang et al.* [2010]

Before testing the lookup table in different atmospheres, we first compare the simulation results of EPMC with the method of ***Fang et al.*** [2010]. Figures 4a and 4b show the comparison of ionization profiles produced by monoenergetic beams of 100 keV and 1 MeV electrons with an isotropic pitch angle distribution. This comparison is performed for the two MSIS atmospheres utilized in ***Fang et al.*** [2010]: atmosphere 1 with $F_{10.7}$ = 50 sfu and A_p = 5 nT, and atmosphere 2 with $F_{10.7}$ = 300 sfu and A_p = 65 nT. The ionization profiles produced by 100-keV and 1-MeV electrons, but with a sine pitch angle distribution, are plotted as blue solid and dashed lines. The precipitation source is assumed to have a total energy flux of 1 erg/cm^2/s. Figures 4c and 4d show similar results, but for precipitation electrons with an exponential energy distribution with the characteristic energy ε_0 being 100 keV or 300 keV.

For the sake of direct comparison, the magnetic mirroring force is turned off in this set of simulations since it is not considered in ***Fang et al.*** [2010]. As shown in Figure 4, the altitude of peak ionization calculated using the EPMC model is close to the parameterization method of ***Fang et al.*** [2010]. However, EPMC simulation tends to predict more ionization production at relatively higher altitudes. The difference in total ionization between these two methods is, on average, ~19% for monoenergetic beams and 21% for the exponential distribution. The difference for monoenergetic beams is similar to what we reported in ***Xu et al.*** [2018]. This discrepancy is not unacceptable since different electron transport models are employed; the stopping power is different; and different approaches are used to describe the angular diffusion of precipitation beam: ***Fang et al.*** [2010] used a two-stream model for electrons with energies above 50 keV and another multi-stream

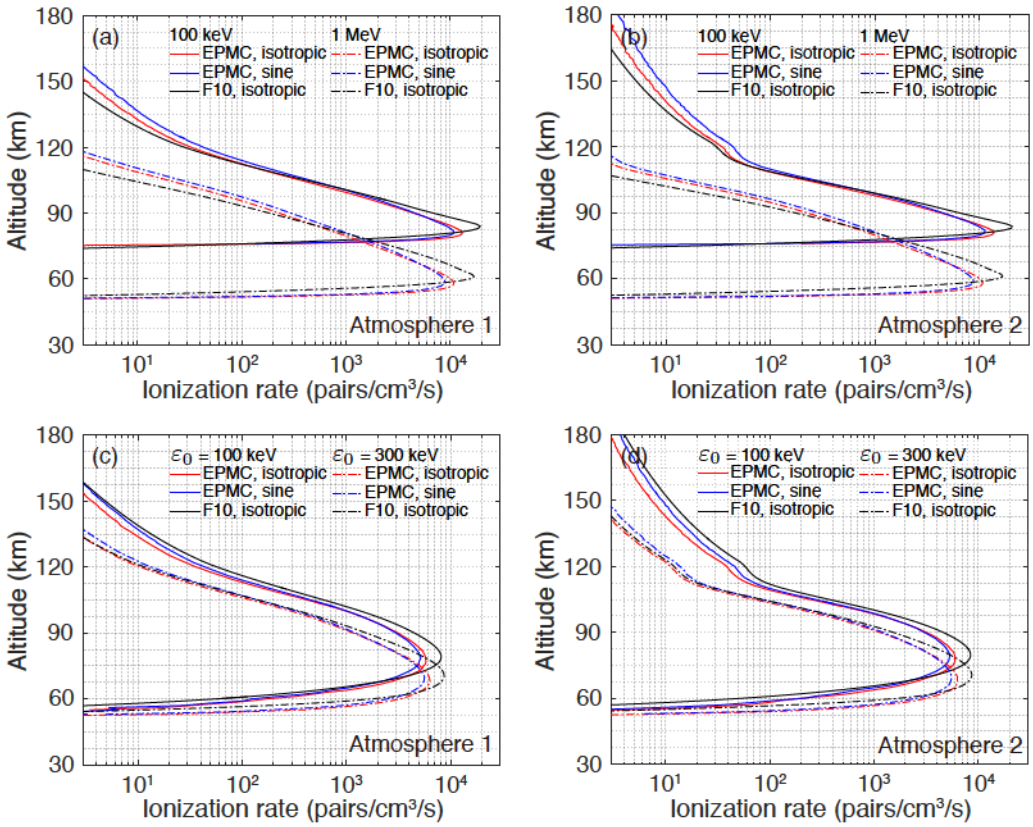

403 **Figure 4.** Comparison of ionization profiles produced by monoenergetic beam of 100 keV and 1 MeV
404 electrons with an isotropic pitch angle distribution between present Monte Carlo simulations (denoted as
405 EPMC in the legend) and the parameterization method of ***Fang et al.*** [2010] (denoted as F10 in the legend).
406 This comparison is performed for two different MSIS atmospheres: (a) atmosphere 1 with $F_{10.7}$ = 50 sfu
407 and A_p = 5 nT; (b) atmosphere 2 with $F_{10.7}$ = 300 sfu and A_p = 65 nT. The ionization profiles produced
408 by 100-keV and 1-MeV electrons with a sine pitch angle distribution are plotted as blue solid and dashed
409 lines, respectively. The precipitation source is assumed to have a total energy flux of 1 erg/cm^2/s. The bottom
410 panels show similar results, but for precipitation electrons with an exponential energy distribution with the
411 characteristic energy ε_0 being 100 keV or 300 keV.

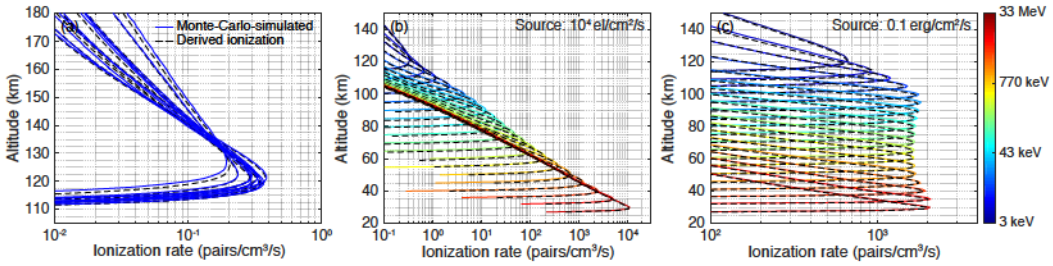

Figure 5. Comparison between direct Monte Carlo results and ionization profiles derived from the lookup table. (a) Ionization production by 3 keV electrons in 10 different MSIS atmospheric profiles. (b) Ionization production by 19 precipitation energies in a fixed background atmosphere. (c) Similar to panel (b), but normalized so that the source precipitation flux is 0.1 erg/cm^2/s.

model for energies below 50 keV, whereas EPMC uses the method of small-angle collisions consistently for all energies [***Lehtinen***, 2000, pp. 15–18].

We have also calculated the ionization profiles produced by a sine pitch angle distribution, and computed the difference from the isotropic distribution. A sine pitch angle distribution contains a smaller portion of electrons within the loss cone and, thus, precipitating electrons deposit less energy in the atmosphere, especially at lower altitudes. For monoenergetic beams, when compared to the sine distribution, an isotropic distribution leads to 22% more ionization around the peak, and 10% more ionization in total. The difference in the altitude of peak ionization is 1 km. For the exponential energy distribution, the difference between these two pitch angle distributions is 13% and 11% in peak and total ionization, respectively. These differences roughly represent the uncertainty of NO_x and HO_x production in chemistry simulation due to the pitch angle distribution. It is important to note that we have only examined several sets of background atmosphere and precipitation distribution here; the difference mentioned above could be notably enhanced under certain precipitation conditions. For example, in a separate test, we found that, if one only considers the data recorded by the 0° telescope onboard POES as the precipitation flux and if the true pitch angle distribution is sine, this could underestimate the peak ionization altitude by ~2 km and the peak ionization rate by almost one order of magnitude. Similar conclusions have also been found by ***Tyssøy et al.*** [2019].

3.2 Monoenergetic Electrons

The validation results of monoenergetic tests are summarized in Figures 5 and 6. Figure 5a shows the comparison of ionization profile produced by 3 keV electrons in 10 different MSIS atmospheres between Monte-Carlo-simulated and derived results, while Figure 5b shows the comparison for 19 electron energies in a fixed background atmosphere. These 10 profiles are randomly chosen from the 100 MSIS atmospheres (Figure 3e) used in validation test. To better compare the ionization rate around the peak, the ionization curves are also normalized so that the source precipitation flux is 0.1 erg/cm^2/s and shown in Figure 5c.

Due to the variation in background atmospheric density, the altitude profiles of ionization production by 3 keV electrons vary dramatically in different runs as shown in Figure 5a. Nevertheless, our method very well captures this range of variation and the largest difference in peak ionization altitude is 1 km. For the other 18 energies, the derived penetration depth is also consistent with the truth as evident in Figures 5b and 5c. The precipitation energy of 3 keV presented in Figure 5a is among the lowest energy of interest

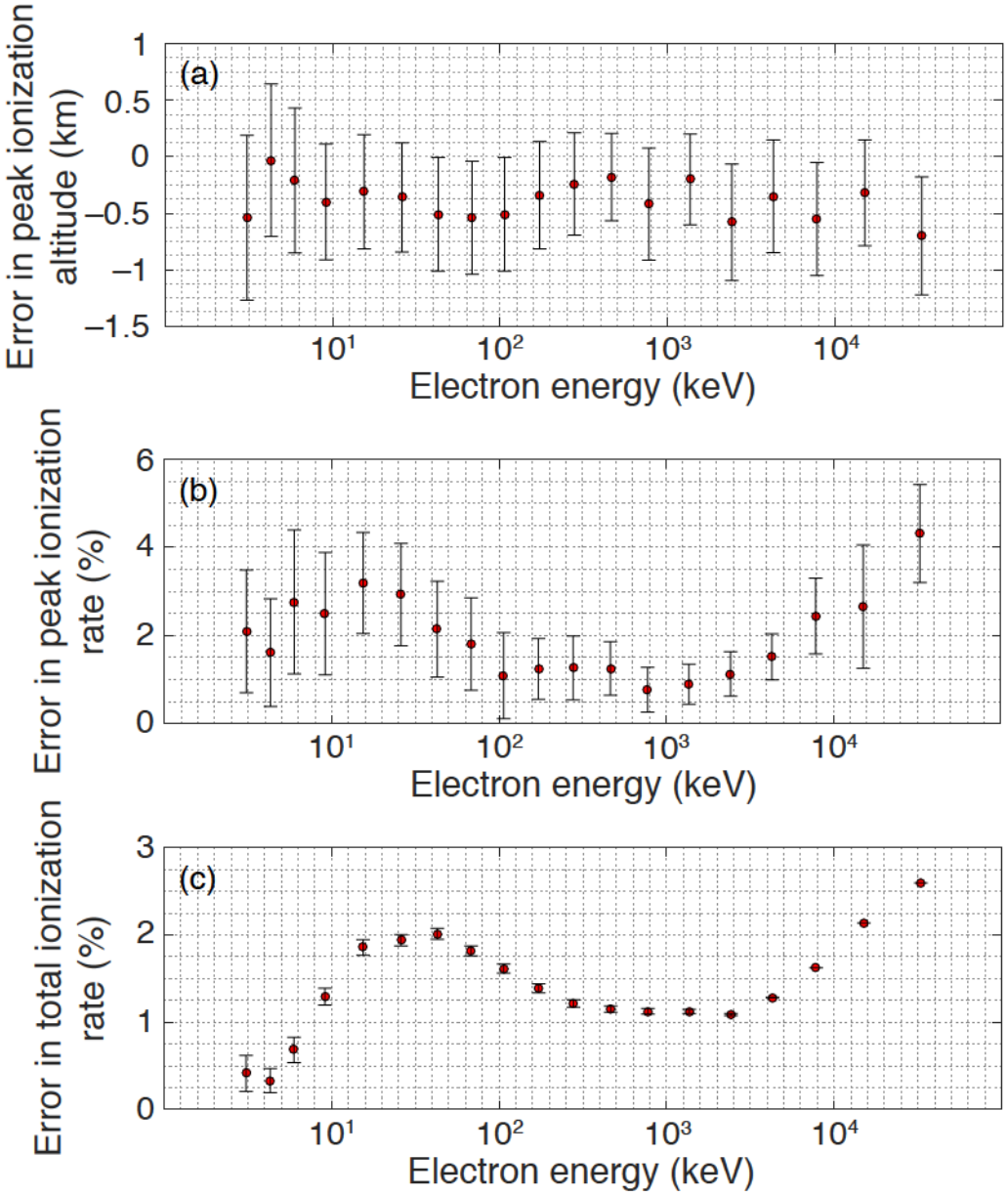

458 **Figure 6.** Error in (a) peak ionization altitude, (b) peak ionization rate, and (c) total ionization rate esti-
459 mated using monoenergetic beams of precipitating electrons and 100 MSIS atmospheric profiles. The error
460 bars show one standard deviation.

for chemistry studies [e.g., ***Mironova et al.***, 2015] and represents the worst-case scenario in error analysis.

The estimated error in peak ionization altitude, peak ionization rate, and total ionization rate is presented in Figure 6. These results are obtained using 100 Monte-Carlo runs for each electron energy; each run uses a background MSIS atmosphere and yields an estimate of the error; we compute the difference in peak altitude, and percentage difference in peak rate and total ionization; the mean errors are denoted as red points in Figure 6; the error bars show one standard deviation. The largest error in peak altitude is −0.7 km at the electron energy of ~33 MeV with a standard deviation of ~0.52 km. In 58% of 1,900 tests (19 electron energies and 100 MSIS atmospheres), the peak altitude of the derived ionization profile turns out to be the same as the truth. Of note, the resolution of ionization profiles is 1 km in altitude and, in majority of these tests, our method can pinpoint the true peak within one grid cell.

The largest error is approximately 4.3% in peak ionization rate, and 2.6% in total ionization rate, both at the energy of 33 MeV. As noted, we predetermine the lowest altitude of ionization before performing interpolation and this allows a good estimation of total ionization in the new atmosphere. For this reason, the errors in total ionization are overall smaller than 3%. However, as explained above, the column mass density above the predetermined lowest altitude of ionization in the new atmosphere is slightly larger than that in the reference atmosphere. In this regard, the altitude of peak ionization in the derived ionization profile is found to be lower than the truth (Figure 6a). The errors in the total ionization are related to how much larger the column mass density in the new atmosphere is than that in the reference atmosphere. The standard deviation of the total ionization is controlled by how variable the column mass density is around the lowest ionization altitudes. For example, the column mass density above 50 km does not vary significantly for the 100 background atmospheres and this is why the error bars are much smaller at energies greater than 2 MeV in Figure 6c. It is expected that, with a finer altitude resolution, the errors shown in Figure 6 could become even smaller.

3.3 Exponential Energy Distribution and Isotropic Pitch Angle Distribution

In addition to monoenergetic beams, we have tested exponential energy distributions. Figure 7 shows the comparison between direct Monte Carlo results and ionization profiles derived from the lookup table. For context, source precipitating electrons in this set of tests are assumed to have an exponential distribution in energy and an isotropic distribution in pitch angle; a total of 2,100 validation tests are performed using 21 ε_0 values and 100 MSIS atmospheric profiles. To illustrate the effectiveness of our method, we plot the ionization profiles in 5 randomly-picked atmospheres; the background mass density profiles of these atmospheres are shown in Figure 7f. For each atmosphere, the 5 ε_0 values that are equally spaced in logarithmic scale between 10 keV and 1 MeV are shown (10 keV, 32 keV, 100 keV, 317 keV, and 1 MeV).

For different combinations of MSIS atmosphere and ε_0 value, the derived ionization profiles show excellent agreements with the truth data in terms of the overall trend and ionization peak. The slight difference at altitudes above ~160 km is likely due to the numerical error that we explain in section 2.5. We emphasize that the choice of the most energetic beam ($\varepsilon_{\max}$) in equation 1 is critical in this comparison in that it controls the magnitude of ionization rate at the lowest altitudes. Although we assume an energy range of 10 keV to 10 MeV, due to the limited number of particles, the highest energy of electrons generated in Monte Carlo runs is usually lower than 10 MeV. In these comparisons, $\varepsilon_{\max}$ is specifically set to be the highest energy of source electrons in Monte Carlo runs.

Figure 8 shows the corresponding error in peak ionization altitude, peak ionization rate, and total ionization for different ε_0 values (x axis) and MSIS atmosphere (y axis). The errors shown in Figures 8b and 8c are the absolute value of percentage difference be-

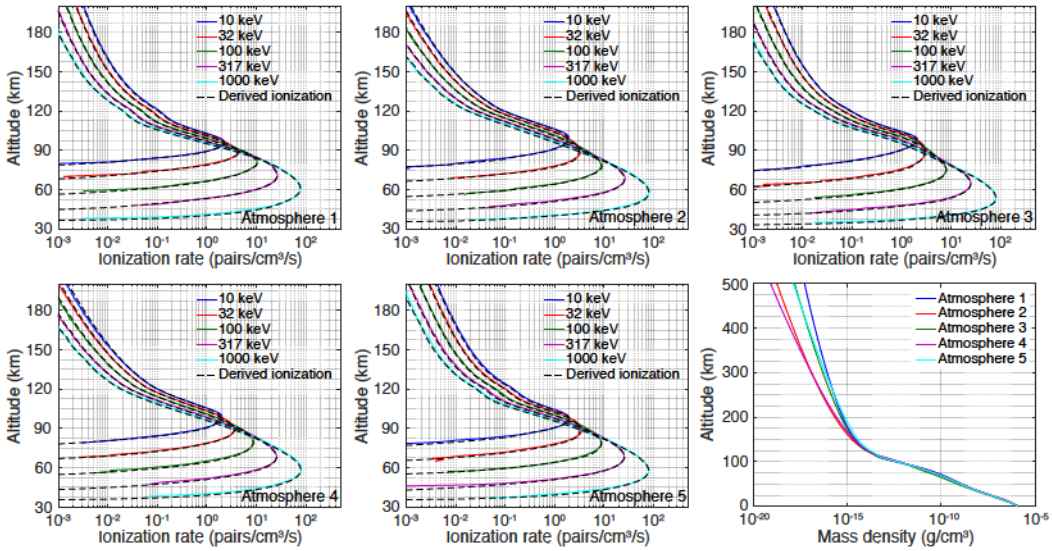

Figure 7. Comparison between direct Monte Carlo results and ionization profiles derived from the lookup table. Source precipitating electrons are assumed to have an exponential distribution in energy and an isotropic distribution in pitch angle. 21 characteristic energies (ε_0) and 100 MSIS atmosphere are used in this set of tests. We show the comparison in 5 randomly-picked atmospheres to illustrate the effectiveness of our method. For each atmosphere, the 5 ε_0 values that are equally spaced in logarithmic scale between 10 keV and 1 MeV are shown. The bottom right panel shows the mass density of these atmospheres.

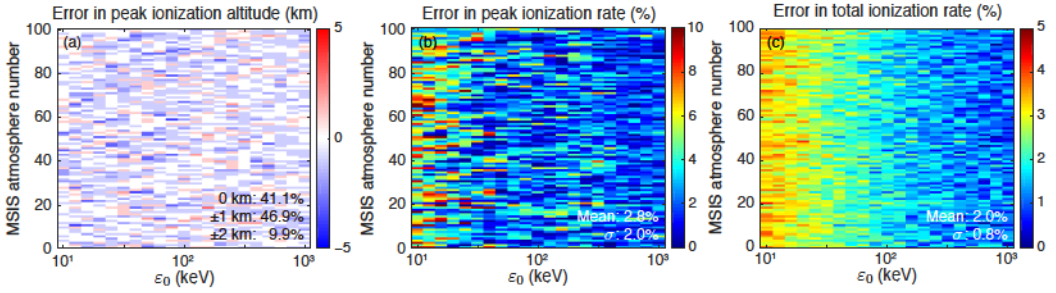

Figure 8. Error in (a) peak ionization altitude, (b) peak ionization rate, and (c) total ionization estimated using precipitating electrons with an exponential distribution in energy and an isotropic distribution in pitch angle, and 100 MSIS atmospheric profiles (y axis). The ε_0 values used for the exponential energy distribution are shown as the x axis.

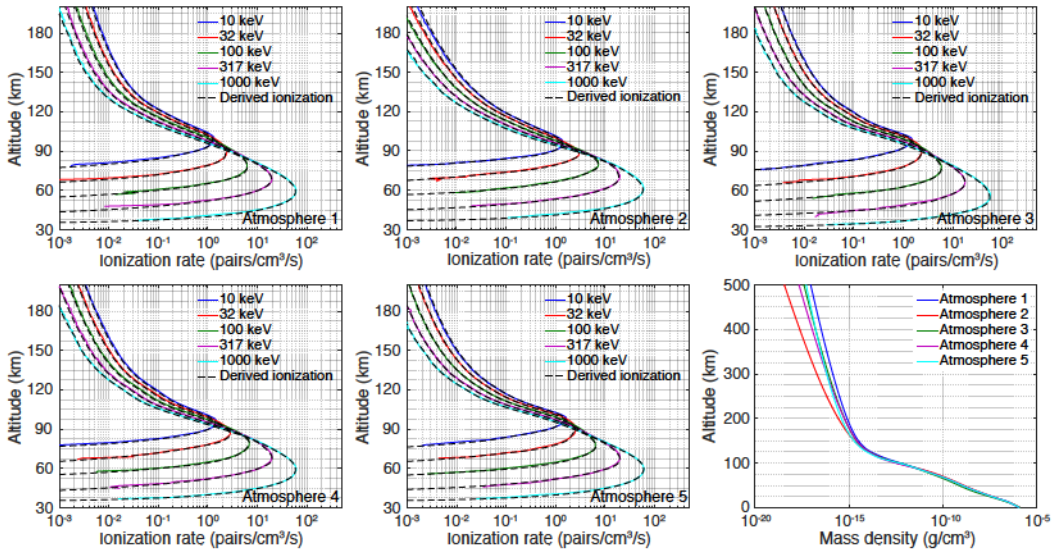

554 **Figure 9.** Similar to Figure 7, but calculated using precipitating electrons with a sine distribution in pitch
555 angle.

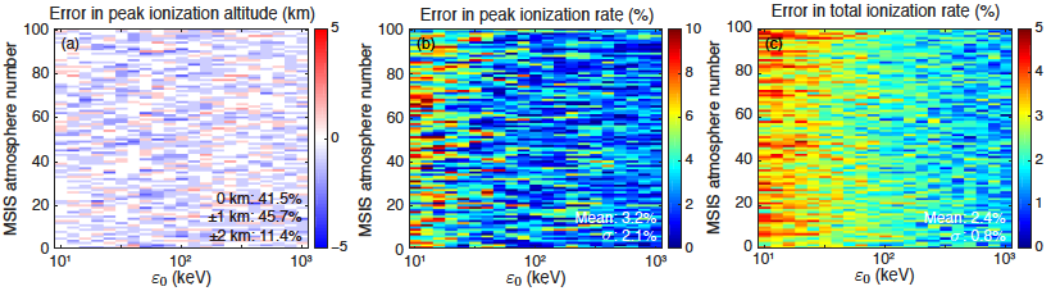

556 **Figure 10.** Similar to Figure 8, but calculated using precipitating electrons with a sine distribution in pitch
557 angle.

537 tween the derived and true ionization profile. These errors are reasonably small and con-
538 sistent with the percentage difference presented in Figure 3f, indicating that our method
539 has satisfactorily estimated the true ionization in 2,100 tests. In 41% of all the tests, the
540 peak altitude of derived ionization is the same as the truth to within 1 km resolution. The
541 difference in peak altitude is found to be ±1 km in 47% of all the tests, and ±2 km in
542 10% of all the tests. As noted above, because of the way we determine the lowest ion-
543 ization altitude, the ionization profile derived from the lookup table tends to bias towards
544 lower peak altitude and larger total ionization value.

545 The mean error and standard deviation are 2.8% and 2% for peak ionization rate,
546 and 2% and 0.8% for total ionization. The largest error in peak ionization rate and total
547 ionization is, respectively, ~13% and ~4.3%. On average, these errors become smaller
548 with increasing ε_0 value because lower ε_0 value contains relatively more low-energy com-
549 ponent, corresponding to more ionization production at higher altitudes, where the ran-
550 domness effects (see section 2.5) are pronounced. If we define good estimation as an error
551 within 1 km in peak altitude and an error of less than 5% in peak ionization rate, the de-
552 rived profiles in 1,807 cases meet this criterion. Our method can accurately estimate the
553 true ionization in ~86% of all the tests.

3.4 Exponential Energy Distribution and Sine Pitch Angle Distribution

Figures 9 and 10 are similar to Figures 7 and 8 above, but the source precipitating electrons have a sine distribution in pitch angle. Satellite-measured pitch angle distributions of precipitation fluxes are poorly resolved primarily due to instrumental challenges. Data from Van Allen Probes show no evidence of discontinuity in pitch angle distribution [e.g., ***Baker et al.***, 2014], and a sine function is believed to be more representative and thus adopted here.

This set of test results is comparable to those of the isotropic distribution (Figures 7 and 8). We observe from Figure 9 that, for the sine distribution, the derived ionization profiles are also remarkably close to the truth. The largest error is 2 km in peak ionization altitude, ~13% in peak ionization rate, and ~5% in total ionization. For the peak ionization rate, the mean error is 3.2% with a fairly large deviation of 2.1%. These values are 2.4% and 0.8% for the total ionization. Among 2,100 tests, the error in peak altitude is found to be 0 km in 42%, ±1 km in 46%, and ±2 km in 11% of all the tests. Our method achieves a good-estimation (≤1 km in peak altitude and ≤5% in peak ionization rate) rate of 82% (1,721 cases). The errors obtained using the sine pitch angle distribution are, on average, larger than those of isotropic distribution because, as explained above, a sine distribution causes more ionization production at relatively higher altitudes, where the numerical error is larger.

4 Discussion and Conclusions

In this study, using Monte Carlo simulations of EEP, we have tabulated the atmospheric ionization response to monoenergetic electrons with different pitch angles and energies between ~3 keV and ~33 MeV. We have quantified the pitch angle dependence, and explained the randomness effects in Monte Carlo simulations at low-density altitudes, as well as the resultant uncertainty in ionization calculation. Based on the parameterization method of ***Fang et al.*** [2010], a robust method has been developed for the specification of ionization production in an arbitrary atmosphere by precipitating electrons with any distribution in electron energy and pitch angle. Moreover, we have validated this method using 100 MSIS atmospheric profiles and different energy and pitch angle distributions.

Among traditional precipitation transport models, although the Monte Carlo technique provides the most detailed simulation, it is usually regarded as computationally intense and unsuitable for routine calculation of ionization profiles in large-scale atmospheric modeling [e.g., ***Solomon***, 2001]. However, tabulating the atmospheric ionization response to all possible combinations of electron energy and pitch angle can effectively remedy this deficiency. In this work, we have demonstrated the feasibility of this lookup table. Based on a total of 6,100 validation tests using monoenergetic and exponential energy distributions, and isotropic and sine pitch angle distributions, this lookup table can satisfactorily estimate the atmospheric ionization produced by EEP, especially at the altitudes of peak ionization. In 91% of all the tests, the error in peak ionization altitude is found to be within 1 km with a mean error of 2.7% in peak ionization rate, and 1.9% in total ionization. In the validation using exponential energy distribution and sine pitch angle distribution, our method can accurately infer (≤1 km in peak altitude and ≤5% in peak ionization rate) the ionization profile in 82% of all the tests. This rate rises to 86% if the pitch angle distribution is isotropic. However, we have only examined this method in the context of Monte Carlo simulations. Further comparison with other electron transport models and real data would be desirable to better calibrate this method.

This method is sufficiently accurate for atmospheric chemistry simulation. The changes in NO_x and HO_x production are roughly proportional to the peak ionization rate. In this regard, the errors found in our validation tests roughly represent the uncertainty in chemistry simulations. In general, these errors are believed to be smaller than other uncertain-

ties in chemistry simulations, for example, reaction and transport rates, and the poorly-investigated abundance of minor species [e.g., ***Verronen***, 2006]. We emphasize that this method is optimized to provide the best guess of ionization production around the peak (see section 2.3) because this part contributes most to chemical changes; the error could be as large as ~20% for ionization rate at altitudes above 200 km. If the main focus is ionization rate in the E- and F-region ionosphere, this method needs to be used with extra caution.

Different from prior parameterization schemes, this method fully accounts for the dependence of ionization production on the atmospheric conditions and on the electron energy and pitch angle distribution. It is applicable to any Earth's atmospheric condition and highly suitable to incorporate spacecraft measurements into atmospheric chemistry models with few limitations. Of note, the lookup table reported here is specifically constructed for electron pitch angles with respect to the background magnetic field, whereas space-borne instruments usually record fluxes from a given solid angle. This difference needs to be properly taken into account in future analysis. Moreover, the initial altitude of this lookup table may be different from many EEP-observing satellites, for example, POES. To directly apply this table to the analysis of POES data, one needs to first map the precipitation fluxes measured by POES from its location to the altitude of 500 km using the background geomagnetic field. The key factors to obtain an accurate ionization profile are the most energetic beam in equation 1, as noted above, and the smoothness of energy and pitch angle distribution. Space-borne measurements of precipitation fluxes usually have limited resolution in energy and pitch angle. If the input energy or/and pitch angle distribution is discontinuous at a given value, the derived ionization profile may exhibit some stepwise changes at the corresponding altitude.

Quantifying the atmospheric effects brought by EEP has been challenging for several decades and this is partially because of the accuracy in ionization source in chemistry modeling. Recent studies have gradually recognized the importance of considering precipitation fluxes in the full range of energy and pitch angle [***Randall et al.***, 2015; ***Nesse Tyssøy et al.***, 2016; ***Smith-Johnsen et al.***, 2018; ***Pettit et al.***, 2019]. It is from this perspective that we extend the parameterization method of ***Fang et al.*** [2010] by expanding the energy range and including the pitch angle dependence, and establish a generalized method for the specification of EEP-produced ionization profile. Validation results show that this method provides a reliable means to convert space-borne measurements of precipitation fluxes into ionization input in atmospheric chemistry models, thereby assisting model-observation comparison and better quantification of atmospheric effects induced by EEP.

Acknowledgments

This research was supported by the NSF grants AGS-1243176 and AGS-1732359. Hilde Nesse Tyssøy is supported by the Norwegain Research Council (NRC) under CoE contract 223252 and the U.S.–Norway Fulbright Foundation for Educational Exchange. The simulation data and analysis codes used to generate all figures and results in this paper, as well as the code developed for the calculation of atmospheric ionization, are available at https://doi.org/10.5281/zenodo.3945306.

References

Andersson, M. E., P. T. Verronen, C. J. Rodger, M. A. Clilverd, and A. Seppälä (2013), Missing driver in the Sun-Earth connection from energetic electron precipitation impacts mesospheric ozone, ***Nat. Commun.***, *5*, 5197–5197, doi:10.1038/ncomms6197.

Artamonov, A., I. Mironova, G. Kovaltsov, A. Mishev, E. Plotnikov, and N. Konstantinova (2017), Calculation of atmospheric ionization induced by electrons with non-vertical

657 precipitation: Updated model CRAC-EPII, ***Advances in Space Research***, ***59***, 2295–2300.
658 Artamonov, A. A., A. L. Mishev, and I. G. Usoskin (2016), Model CRAC: EPII for at-
659 mospheric ionization due to precipitating electrons: Yield function and applications, ***J.***
660 ***Geophys. Res. Space Physics***, ***121***, 1736–1743.
661 Baker, D. N., C. A. Barth, K. E. Mankoff, S. G. Kanekal, S. M. Bailey, G. M. Mason,
662 and J. E. Mazur (2001), Relationships between precipitating auroral zone electrons and
663 lower thermospheric nitric oxide densities: 1998–2000, ***J. Geophys. Res. Space Physics***,
664 ***106***(A11), 24,465–24,480.
665 Baker, D. N., A. N. Jaynes, V. C. Hoxie, R. M. Thorne, J. C. Foster, X. Li, J. F. Fennell,
666 J. R. Wygant, S. G. Kanekal, P. J. Erickson, et al. (2014), An impenetrable barrier to
667 ultrarelativistic electrons in the van allen radiation belts, ***Nature***, ***515***, 531–534.
668 Barth, C. A., K. D. Mankoff, S. M. Bailey, and S. C. Solomon (2003), Global observa-
669 tions of nitric oxide in the thermosphere, ***J. Geophys. Res. Space Physics***, ***108***(A1).
670 Berger, M. J., and S. M. Seltzer (1972), Bremsstrahlung in the atmosphere, ***J. Atmos. Terr.***
671 ***Phys.***, ***34***(1), 85–108.
672 Breneman, A. W., et al. (2017), Observations directly linking relativistic electron mi-
673 crobursts to whistler mode chorus: Van Allen Probes and FIREBIRD II, ***Geophys. Res.***
674 ***Lett.***, ***44***, 11–265.
675 Callis, L. B., M. Natarajan, J. D. Lambeth, and D. N. Baker (1998), Solar atmospheric
676 coupling by electrons (SOLACE): 2. Calculated stratospheric effects of precipitat-
677 ing electrons, 1979–1988, ***J. Geophys. Res. Atmos.***, ***103***(D21), 28,421–28,438, doi:
678 10.1029/98JD02407.
679 Carron, N. J. (2006), ***An introduction to the passage of energetic particles through matter***,
680 CRC Press.
681 Cotts, B. R. T. (2011), Global quantification of lightning-induced electron precipitation
682 using very low frequency remote sensing, Ph.D. thesis, Stanford Univ., Stanford, CA.
683 Crew, A. B., et al. (2016), First multipoint in situ observations of electron microbursts:
684 Initial results from the NSF FIREBIRD II mission, ***J. Geophys. Res. Space Physics***, ***121***,
685 5272–5283.
686 Fang, X., C. E. Randall, D. Lummerzheim, S. C. Solomon, M. J. Mills, D. R. Marsh,
687 C. H. Jackman, W. Wang, and G. Lu (2008), Electron impact ionization: A new pa-
688 rameterization for 100 eV to 1 MeV electrons, ***J. Geophys. Res.***, ***113***, A09311.
689 Fang, X., C. E. Randall, D. Lummerzheim, W. Wang, G. Lu, S. C. Solomon, and R. A.
690 Frahm (2010), Parameterization of monoenergetic electron impact ionization, ***Geophys.***
691 ***Res. Lett.***, ***37***, L22106, doi:10.1029/2010GL045406.
692 Lazarev, V. I. (1967), Absorption of the energy of an electron beam in the upper atmo-
693 sphere, ***Geomagn. Aeron.***, ***7***, 219.
694 Lehtinen, N. G. (2000), Relativistic runaway electrons above thunderstorms, Ph.D. thesis,
695 Stanford Univ., Stanford, CA.
696 Lehtinen, N. G., T. F. Bell, and U. S. Inan (1999), Monte Carlo simulation of runaway
697 MeV electron breakdown with application to red sprites and terrestrial gamma ray
698 flashes, ***J. Geophys. Res.***, ***104***(A11), 24,699–24,712, doi:10.1029/1999JA900335.
699 Lummerzheim, D. (1992), Comparison of energy dissipation functions for high energy
700 auroral electron and ion precipitation, ***Rep. UAG-R-318***, pp. Geophys. Inst., Univ. of
701 Alaska Fairbanks, Fairbanks.
702 Lyons, L. R., and R. M. Thorne (1973), Equilibrium structure of radiation belt electrons,
703 ***J. Geophys. Res.***, ***78***(13), 2142–2149, doi:10.1029/JA078i013p02142.
704 Marsh, D. R., R. R. Garcia, D. E. Kinnison, B. A. Boville, F. Sassi, S. C. Solomon, and
705 K. Matthes (2007), Modeling the whole atmosphere response to solar cycle changes in
706 radiative and geomagnetic forcing, ***J. Geophys. Res.***, ***112***, D23306.
707 Marshall, R. A., and J. Bortnik (2018), Pitch Angle Dependence of Energetic Electron
708 Precipitation: Energy Deposition, Backscatter, and the Bounce Loss Cone, ***J. Geophys.***
709 ***Res. Space Physics***, ***123***, 2412–2423.

Marshall, R. A., and C. M. Cully (2020), Atmospheric effects and signatures of high-energy electron precipitation, in ***The Dynamic Loss of Earth's Radiation Belts***, pp. 199–255, Elsevier.

Marshall, R. A., M. Nicolls, E. Sanchez, N. G. Lehtinen, and J. Neilson (2014), Diagnostics of an artificial relativistic electron beam interacting with the atmosphere, ***J. Geophys. Res. Space Physics***, ***119***, 8560–8577.

Marshall, R. A., W. Xu, A. Sousa, M. McCarthy, and R. Millan (2019), X-ray signatures of lightning-induced electron precipitation, ***J. Geophys. Res. Space Physics***, ***124***, 10,230–10,245, doi:10.1029/2019JA027044.

Marshall, R. A., W. Xu, T. Woods, C. Cully, A. Jaynes, C. Randall, D. Baker, M. McCarthy, H. E. Spence, G. Berland, et al. (2020), The aepex mission: Imaging energetic particle precipitation in the atmosphere through its bremsstrahlung x-ray signatures, ***Advances in Space Research***, ***66***(1), 66–82.

Mironova, I. A., K. L. Aplin, F. Arnold, G. A. Bazilevskaya, R. G. Harrison, A. A. Krivolutsky, K. A. Nicoll, E. V. Rozanov, E. Turunen, and I. G. Usoskin (2015), Energetic particle influence on the earth's atmosphere, ***Spa. Sci. Rev.***, ***194***, 1–96.

Nesse Tyssøy, H., M. I. Sandanger, L.-K. Ødegaard, J. Stadsnes, A. Aasnes, and A. Zawedde (2016), Energetic electron precipitation into the middle atmosphere–Constructing the loss cone fluxes from MEPED POES, ***J. Geophys. Res. Space Physics***, ***121***, 5693–5707.

Pettit, J. M., C. E. Randall, E. D. Peck, D. R. Marsh, M. van de Kamp, X. Fang, V. L. Harvey, C. J. Rodger, and B. Funke (2019), Atmospheric effects of > 30-kev energetic electron precipitation in the southern hemisphere winter during 2003, ***J. Geophys. Res. Space Physics***, ***124***, 8138–8153.

Picone, J. M., A. E. Hedin, D. P. Drob, and A. C. Aikin (2002), NRLMSISE-00 empirical model of the atmosphere: Statistical comparisons and scientific issues, ***J. Geophys. Res.***, ***107***(A12), 1468, doi:10.1029/2002JA009430.

Randall, C. E., V. L. Harvey, L. A. Holt, D. R. Marsh, D. Kinnison, B. Funke, and P. F. Bernath (2015), Simulation of energetic particle precipitation effects during the 2003–2004 Arctic winter, ***J. Geophys. Res. Space Physics***, ***120***, 5035–5048.

Randall, C. E., et al. (2007), Energetic particle precipitation effects on the Southern Hemisphere stratosphere in 1992–2005, ***J. Geophys. Res.***, ***112***, D08308, doi:10.1029/2006JD007696.

Rees, M. H. (1989), ***Physics and Chemistry of the Upper Atmosphere***, Cambridge Univ. Press, New York.

Roble, R. G., and E. C. Ridley (1987), An auroral model for the NCAR thermospheric general circulation model (TGCM), ***Ann. Geophys.***, ***5A***, 369–382.

Rozanov, E., M. Calisto, T. Egorova, T. Peter, and W. Schmutz (2012), Influence of the precipitating energetic particles on atmospheric chemistry and climate, ***Surv. Geophys.***, ***33***, 483–501, doi:10.1007/s10712-012-9192-0.

Rusch, D. W., J.-C. Gerard, S. Solomon, P. J. Crutzen, and G. C. Reid (1981), The effect of particle precipitation events on the neutral and ion chemistry of the middle atmosphere–I. Odd nitrogen, ***Planet. Space Sci.***, ***29***(7), 767–774, doi:10.1016/0032-0633(81)90048-9.

Sinnhuber, M., H. Nieder, and N. Wieters (2012), Energetic particle precipitation and the chemistry of the mesosphere/lower thermosphere, ***Surv. Geophys.***, ***33***, 1281–1334, doi:10.1007/s10712-012-9201-3.

Smith-Johnsen, C., D. R. Marsh, Y. Orsolini, H. Nesse Tyssøy, K. Hendrickx, M. I. Sandanger, L.-K. G. Ødegaard, and F. Stordal (2018), Nitric oxide response to the April 2010 electron precipitation event: Using WACCM and WACCM-D with and without medium-energy electrons, ***J. Geophys. Res. Space Physics***, ***123***, 5232–5245.

Solomon, S., D. W. Rusch, J.-C. Gérard, G. C. Reid, and P. J. Crutzen (1981), The effect of particle precipitation events on the neutral and ion chemistry of the middle atmosphere: II. Odd hydrogen, ***Planet. Space Sci.***, ***29***(8), 885–893, doi:10.1016/0032-

0633(81)90078-7.

Solomon, S. C. (2001), Auroral particle transport using monte carlo and hybrid methods, *J. Geophys. Res.*, *106*(A1), 107–116, doi:10.1029/2000JA002011.

Spencer, L. V. C. (1959), ***Energy dissipation by fast electrons***, vol. 1, US Department of Commerce, National Bureau of Standards.

Thorne, R. M. (1980), The importance of energetic particle precipitation on the chemical composition of the middle atmosphere, ***PAGEOPH***, *118*, 128–151, doi: 0.1007/BF01586448.

Tyssøy, H. N., A. Haderlein, M. Sandanger, and J. Stadsnes (2019), Intercomparison of the POES/MEPED loss cone electron fluxes with the CMIP6 parametrization, ***J. Geophys. Res. Space Physics***, *124*, 628–642.

Vampola, A. (1997), Outer zone energetic electron environment update, in ***Conference on the High Energy Radiation Background in Space. Workshop Record***, pp. 128–136, IEEE.

Verronen, P. T. (2006), Ionosphere-atmosphere interaction during solar proton events, Ph.D. thesis, Univ. of Helsinki, Helsinki, Finland.

Whittaker, I. C., R. J. Gamble, C. J. Rodger, M. A. Clilverd, and J.-A. Sauvaud (2013), Determining the spectra of radiation belt electron losses: Fitting demeter electron flux observations for typical and storm times, ***J. Geophys. Res. Space Physics***, *118*, 7611–7623.

Xu, W., and R. A. Marshall (2019), Characteristics of Energetic Electron Precipitation Estimated from Simulated Bremsstrahlung X-ray Distributions, ***J. Geophys. Res. Space Physics***, *124*, 2831–2843.

Xu, W., R. A. Marshall, X. Fang, E. Turunen, and A. Kero (2018), On the Effects of Bremsstrahlung Radiation During Energetic Electron Precipitation, ***Geophys. Res. Lett.***, *45*(2), 1167–1176.